Draft version April 23, 2013
Preprint typeset using LaTeX style emulateapj v. 5/2/11

arXiv:1304.5559v1 [astro-ph.HE] 19 Apr 2013

IMPULSIVE AND LONG DURATION HIGH-ENERGY GAMMA-RAY EMISSION FROM THE VERY BRIGHT 2012 MARCH 7 SOLAR FLARES

M. Ajello[2], A. Albert[3], A. Allafort[4], L. Baldini[5], G. Barbiellini[6,7], D. Bastieri[8,9], R. Bellazzini[10], E. Bissaldi[11], E. Bonamente[12,13], T. J. Brandt[14], J. Bregeon[10], M. Brigida[15,16], P. Bruel[17], R. Buehler[18], S. Buson[8,9], G. A. Caliandro[19], R. A. Cameron[4], P. A. Caraveo[20], C. Cecchi[12,13], E. Charles[4], A. Chekhtman[21], J. Chiang[4], G. Chiaro[9], S. Ciprini[22,23], R. Claus[4], J. Cohen-Tanugi[24], L. R. Cominsky[25], J. Conrad[26,27,28,29], S. Cutini[22,23], F. D'Ammando[30], F. de Palma[15,16], C. D. Dermer[31], R. Desiante[6], S. W. Digel[4], E. do Couto e Silva[4], P. S. Drell[4], A. Drlica-Wagner[4], C. Favuzzi[15,16], W. B. Focke[4], A. Franckowiak[4], Y. Fukazawa[32], P. Fusco[15,16], F. Gargano[16], D. Gasparrini[22,23], S. Germani[12,13], N. Giglietto[15,16], P. Giommi[22], F. Giordano[15,16], M. Giroletti[30], T. Glanzman[4], G. Godfrey[4], I. A. Grenier[33], J. E. Grove[31], S. Guiriec[14], D. Hadasch[19], M. Hayashida[4,34], E. Hays[14], D. Horan[17], X. Hou[35], R. E. Hughes[3], Y. Inoue[4], M. S. Jackson[36,27], T. Jogler[4], G. Jóhannesson[37], A. S. Johnson[4], W. N. Johnson[31], T. Kamae[4], J. Knödlseder[38,39], D. Kocevski[4], M. Kuss[10], J. Lande[4], S. Larsson[26,27,40], L. Latronico[41], F. Longo[6,7], F. Loparco[15,16], B. Lott[35], M. N. Lovellette[31], P. Lubrano[12,13], M. Mayer[18], M. N. Mazziotta[16], J. E. McEnery[14,42], P. F. Michelson[4], T. Mizuno[43], A. A. Moiseev[44,42], C. Monte[15,16], M. E. Monzani[4], A. Morselli[45], I. V. Moskalenko[4], S. Murgia[4], T. Nakamori[46], R. Nemmen[14], E. Nuss[24], M. Ohno[47], T. Ohsugi[43], N. Omodei[4,1], M. Orienti[30], E. Orlando[4], J. F. Ormes[48], D. Paneque[49,4], J. H. Panetta[4], J. S. Perkins[14,50,44,51], M. Pesce-Rollins[10,1], V. Petrosian[4,1], F. Piron[24], G. Pivato[9], T. A. Porter[4,4], S. Rainò[15,16], R. Rando[8,9], M. Razzano[10,52], A. Reimer[11,4], O. Reimer[11,4], M. Roth[53], A. Schulz[18], C. Sgrò[10], E. J. Siskind[54], G. Spandre[10], P. Spinelli[15,16], H. Takahashi[32], J. G. Thayer[4], J. B. Thayer[4], D. J. Thompson[14], L. Tibaldo[4], M. Tinivella[10], G. Tosti[12,13], E. Troja[14,55], T. L. Usher[4], J. Vandenbroucke[4], V. Vasileiou[24], G. Vianello[4,56], V. Vitale[45,57], M. Werner[11], B. L. Winer[3], D. L. Wood[58], K. S. Wood[31], Z. Yang[26,27]

Draft version April 23, 2013

ABSTRACT

The *Fermi* Large Area Telescope (LAT) observed two bright X-class solar flares on 2012 March 7, and detected gamma-rays up to 4 GeV. We detected gamma-rays both during the impulsive and temporally-extended emission phases, with emission above 100 MeV lasting for approximately 20 hours. Accurate localization of the gamma-ray production site(s) coincide with the solar active region from which X-ray emissions associated with these flares originated. Our analysis of the > 100 MeV gamma-ray emission shows a relatively rapid monotonic decrease in flux during the first hour of the impulsive phase, and a much slower, almost monotonic decrease in flux for the next 20 hours. The spectra can be adequately described by a power law with a high energy exponential cutoff, or as resulting from the decay of neutral pions produced by accelerated protons and ions with an isotropic power-law energy distribution. The required proton spectrum has a number index ~ 3, with minor variations during the impulsive phase, while during the temporally extended phase the spectrum softens monotonically, starting with index ~ 4. The > 30 MeV proton flux and spectra observed near the Earth by the GOES satellites also show a monotonic flux decrease and spectral softening during the extended phase, but with a harder spectrum, with index ~ 3. Based on the *Fermi*-LAT and GOES observations of the flux and spectral evolution of these bright flares, we explore the relative merits of prompt and continuous acceleration scenarios, hadronic and leptonic emission processes, and acceleration at the solar corona by the fast Coronal Mass Ejections (CME) as explanations for the observations. We conclude that the most likely scenario is continuous acceleration of protons in the solar corona which penetrate the lower solar atmosphere and produce pions that decay into gamma-rays.

Subject headings: Gamma rays: observations — Sun —Solar flares — *Fermi* Gamma-ray Space Telescope

[1] Corresponding authors:
N. Omodei, nicola.omodei@stanford.edu;
M. Pesce-Rollins, melissa.pesce.rollins@pi.infn.it;
V. Petrosian, vahep@stanford.edu.
[2] Space Sciences Laboratory, 7 Gauss Way, University of California, Berkeley, CA 94720-7450, USA
[3] Department of Physics, Center for Cosmology and Astro-Particle Physics, The Ohio State University, Columbus, OH 43210, USA
[4] W. W. Hansen Experimental Physics Laboratory, Kavli Institute for Particle Astrophysics and Cosmology, Department of Physics and SLAC National Accelerator Laboratory, Stanford University, Stanford, CA 94305, USA
[5] Università di Pisa and Istituto Nazionale di Fisica Nucleare, Sezione di Pisa I-56127 Pisa, Italy
[6] Istituto Nazionale di Fisica Nucleare, Sezione di Trieste, I-34127 Trieste, Italy
[7] Dipartimento di Fisica, Università di Trieste, I-34127 Trieste, Italy
[8] Istituto Nazionale di Fisica Nucleare, Sezione di Padova, I-35131 Padova, Italy
[9] Dipartimento di Fisica e Astronomia "G. Galilei", Università di Padova, I-35131 Padova, Italy
[10] Istituto Nazionale di Fisica Nucleare, Sezione di Pisa, I-56127 Pisa, Italy
[11] Institut für Astro- und Teilchenphysik and Institut für Theoretische Physik, Leopold-Franzens-Universität Innsbruck, A-6020 Innsbruck, Austria
[12] Istituto Nazionale di Fisica Nucleare, Sezione di Perugia, I-06123 Perugia, Italy

1. INTRODUCTION

Measurements of the long lasting gamma-ray emission from bright solar flares provide the opportunity to investigate the impulsive energy release and acceleration mechanisms responsible for these explosive phenomena. The June 11 1991 Geostationary Operational Satellite Server (GOES) X12.0 class flare observed by the EGRET instrument on-board the Compton Gamma-ray Observatory (Hughes et al. 1980; Kanbach et al. 1988; Thompson et al. 1993; Esposito et al. 1999) produced gamma-rays with energies greater than 100 MeV up to 8 hours after the impulsive phase, setting a record for the detection of long lasting emission of high-energy photons (Kanbach et al. 1993a). The origin of this temporally extended emission is not well understood. Important questions such as whether (i) the radiative process is hadronic or leptonic, (ii) the acceleration happens at the flare site or at the Coronal Mass Ejection (CME), (iii) continuous acceleration or trapping and precipitation are required, are still debated. Additional and more detailed flare observations are clearly necessary to fully understand the mechanisms at work to produce the high-energy gamma-rays.

The *Fermi* observatory is comprised of two instruments: the Large Area Telescope (LAT) designed to detect gamma rays from 20 MeV up to more than 300 GeV (Atwood et al. 2009) and the Gamma-ray Burst Monitor (GBM) which is sensitive from ~ 8 keV up to 40 MeV (Meegan et al. 2009). The orbital inclination of the *Fermi* satellite is 25.6° with an altitude of 565 km and completes one full orbit every 90 minutes.

The LAT has already detected several flares above 100 MeV, during both the impulsive and the temporally extended phases (Ohno et al. 2011; Omodei et al. 2011; Tanaka et al. 2012; Petrosian et al. 2012; Omodei et al. 2012). The first *Fermi* GBM and LAT detection from the impulsive GOES M2.0 flare of June 12 2010 is presented in Ackermann et al. (2012a). The analysis of this flare was performed using the LAT Low-Energy (LLE) technique (see Appendix 3.1) because the soft X-rays emitted during the prompt emission of a flare penetrate the anti-coincidence detector (ACD) of the LAT causing a pile-up effect which can result in a significant decrease in gamma-ray detection efficiency in the standard on-ground photon analysis. The pile-up effect has been addressed in detail and we refer the reader to Ackermann et al. (2012a) and Abdo et al. (2009b) for a full descrip-

[13] Dipartimento di Fisica, Università degli Studi di Perugia, I-06123 Perugia, Italy
[14] NASA Goddard Space Flight Center, Greenbelt, MD 20771, USA
[15] Dipartimento di Fisica "M. Merlin" dell'Università e del Politecnico di Bari, I-70126 Bari, Italy
[16] Istituto Nazionale di Fisica Nucleare, Sezione di Bari, 70126 Bari, Italy
[17] Laboratoire Leprince-Ringuet, École polytechnique, CNRS/IN2P3, Palaiseau, France
[18] Deutsches Elektronen Synchrotron DESY, D-15738 Zeuthen, Germany
[19] Institut de Ciències de l'Espai (IEEE-CSIC), Campus UAB, 08193 Barcelona, Spain
[20] INAF-Istituto di Astrofisica Spaziale e Fisica Cosmica, I-20133 Milano, Italy
[21] Center for Earth Observing and Space Research, College of Science, George Mason University, Fairfax, VA 22030, resident at Naval Research Laboratory, Washington, DC 20375, USA
[22] Agenzia Spaziale Italiana (ASI) Science Data Center, I-00044 Frascati (Roma), Italy
[23] Istituto Nazionale di Astrofisica - Osservatorio Astronomico di Roma, I-00040 Monte Porzio Catone (Roma), Italy
[24] Laboratoire Univers et Particules de Montpellier, Université Montpellier 2, CNRS/IN2P3, Montpellier, France
[25] Department of Physics and Astronomy, Sonoma State University, Rohnert Park, CA 94928-3609, USA
[26] Department of Physics, Stockholm University, AlbaNova, SE-106 91 Stockholm, Sweden
[27] The Oskar Klein Centre for Cosmoparticle Physics, AlbaNova, SE-106 91 Stockholm, Sweden
[28] Royal Swedish Academy of Sciences Research Fellow, funded by a grant from the K. A. Wallenberg Foundation
[29] The Royal Swedish Academy of Sciences, Box 50005, SE-104 05 Stockholm, Sweden
[30] INAF Istituto di Radioastronomia, 40129 Bologna, Italy
[31] Space Science Division, Naval Research Laboratory, Washington, DC 20375-5352, USA
[32] Department of Physical Sciences, Hiroshima University, Higashi-Hiroshima, Hiroshima 739-8526, Japan
[33] Laboratoire AIM, CEA-IRFU/CNRS/Université Paris Diderot, Service d'Astrophysique, CEA Saclay, 91191 Gif sur Yvette, France
[34] Department of Astronomy, Graduate School of Science, Kyoto University, Sakyo-ku, Kyoto 606-8502, Japan
[35] Centre d'Études Nucléaires de Bordeaux Gradignan, IN2P3/CNRS, Université Bordeaux 1, BP120, F-33175 Gradignan Cedex, France
[36] Department of Physics, Royal Institute of Technology (KTH), AlbaNova, SE-106 91 Stockholm, Sweden
[37] Science Institute, University of Iceland, IS-107 Reykjavik, Iceland
[38] CNRS, IRAP, F-31028 Toulouse cedex 4, France
[39] GAHEC, Université de Toulouse, UPS-OMP, IRAP, Toulouse, France
[40] Department of Astronomy, Stockholm University, SE-106 91 Stockholm, Sweden
[41] Istituto Nazionale di Fisica Nucleare, Sezione di Torino, I-10125 Torino, Italy
[42] Department of Physics and Department of Astronomy, University of Maryland, College Park, MD 20742, USA
[43] Hiroshima Astrophysical Science Center, Hiroshima University, Higashi-Hiroshima, Hiroshima 739-8526, Japan
[44] Center for Research and Exploration in Space Science and Technology (CRESST) and NASA Goddard Space Flight Center, Greenbelt, MD 20771, USA
[45] Istituto Nazionale di Fisica Nucleare, Sezione di Roma "Tor Vergata", I-00133 Roma, Italy
[46] Research Institute for Science and Engineering, Waseda University, 3-4-1, Okubo, Shinjuku, Tokyo 169-8555, Japan
[47] Institute of Space and Astronautical Science, JAXA, 3-1-1 Yoshinodai, Chuo-ku, Sagamihara, Kanagawa 252-5210, Japan
[48] Department of Physics and Astronomy, University of Denver, Denver, CO 80208, USA
[49] Max-Planck-Institut für Physik, D-80805 München, Germany
[50] Department of Physics and Center for Space Sciences and Technology, University of Maryland Baltimore County, Baltimore, MD 21250, USA
[51] Harvard-Smithsonian Center for Astrophysics, Cambridge, MA 02138, USA
[52] Santa Cruz Institute for Particle Physics, Department of Physics and Department of Astronomy and Astrophysics, University of California at Santa Cruz, Santa Cruz, CA 95064, USA
[53] Department of Physics, University of Washington, Seattle, WA 98195-1560, USA
[54] NYCB Real-Time Computing Inc., Lattingtown, NY 11560-1025, USA
[55] NASA Postdoctoral Program Fellow, USA
[56] Consorzio Interuniversitario per la Fisica Spaziale (CIFS), I-10133 Torino, Italy
[57] Dipartimento di Fisica, Università di Roma "Tor Vergata", I-00133 Roma, Italy
[58] Praxis Inc., Alexandria, VA 22303, resident at Naval Research Laboratory, Washington, DC 20375, USA

tion. The list of other flares, and the analysis of the first two flares with long lasting high-energy emission (March 7–8 2011 and June 7 2011) is presented in (*Fermi*-LAT collaboration, in preparation).

Here we report on impulsive and long-duration high-energy gamma-ray emission observed by *Fermi* LAT and associated with the intense X-ray solar flares of 2012 March 7. In the next section (§ 2) we present the temporal evolution of soft X-ray and Solar Energetic Particles (SEP) fluxes as measured by GOES; in § 3 we describe the details of the gamma-ray analysis, and finally, in § 4 we discuss and interpret our results.

2. GOES X-RAY AND SOLAR ENERGETIC PARTICLES

On 2012 March 7 two bright X-class flares originating from the active region NOAA AR#:11429 (located at N16E30) erupted within an hour of each other, marking one of the most active days of Solar Cycle 24. The first flare started at 00:02:00 UT and reached its maximum intensity (X5.4) at 00:24:00 UT while the second X1.3 class flare occurred at 01:05:00 UT, reaching its maximum 9 minutes later.

The GOES satellite observed intense X-ray emission beginning at about 00:05:00 UT and lasting for several hours. Moreover, it detected in three energy bands Solar Energetic Particle (SEP) protons originating from these flares. In the top panels of Figures 1 and 2 the GOES X-ray data measured in both 3–25 keV and 1.5–12 keV channels are shown for two time intervals during the flaring episode. GOES soft X-ray light curves usually do not follow the impulsive nature of the activity because they trace the accumulated energy input by the accelerated particles. In general, based on the so-called *Neupert effect* (Neupert 1968) the derivative of these light curves is considered to be a good proxy for the temporal evolution of the accelerated-particle interactions. Figure 1 shows the light curves for the 1.5–12 and 3–25 keV GOES bands, together with their corresponding derivatives. Such derivatives make it clear that the first flare consisted of two impulsive bursts with a duration of a few minutes each while the second flare was composed of only one such pulse. In the top panel of Figure 2, we display the 5-minutes average rate of protons detected by the GOES satellite in three energy bands (30–50 MeV, 50–100 MeV and >100 MeV). Unfortunately the Reuven Ramaty High-Energy Solar Spectroscopic Imager (RHESSI, Lin et al. 2002) was not observing the Sun during this period.

3. *Fermi* GAMMA-RAY DATA

Orbital sunrise for *Fermi* occurred less than six minutes after the peak of the first flare, triggering the GBM at 00:30:32.129 UT (causing the abrupt rate increase visible in Figure1, middle panel). The second flare is also clearly visible in the BGO_0 detector of the GBM[59]. The *Fermi* LAT >100 MeV count rate[60] was dominated by the gamma-ray emission from the Sun[61], which was nearly 100 times brighter than the Vela Pulsar in the same energy range. During the impulsive phase (the first eighty minutes) the X5.4 flare was so intense that the LAT anti-coincidence detector suffered from pulse pileup(see Appendix A), so the standard instrument response functions (IRFs) could not be used. Instead, the spectral analysis performed for the first 80 minutes differs from that used at later times; moreover, we exclude the impulsive phase from the localization analysis.

To limit the possible bias due to the so-called "fish-eye" effect (Ackermann et al. 2012b, §6.4) we used the true position of the Sun when it was in the field of view of the LAT to calculate an energy and angle-dependent correction that was applied to the reconstructed photon direction on an event-by-event basis.

3.1. *The impulsive phase*

The first step in our analysis of the impulsive phase is to consider 9 adjacent time intervals of LLE data (see Appendix A for a detailed description of the LLE technique). In particular, we included data for the region centered on the Sun at the time corresponding to the middle of each time interval and selected the intervals when the Sun was within 70° from the LAT boresight. For each time interval, we extract two sets of background LLE data at 30 orbits before and after the flare, when *Fermi* was at a similar geomagnetic location. At ±30 orbits (∼2 days) the location and attitude of the spacecraft are approximately the same as during the impulsive phase of the flare. To compensate for the rotation of the Earth, the center of the region of interest (ROI) is held fixed in instrument coordinates at the center of each time bin. This last step is needed to average the two background data sets because the local cosmic-ray-induced background dominates the in-aperture celestial background. In this way we obtain 9 source spectra and 9 background spectra (one for each time interval during the impulsive phase analysis). We compute the LLE energy redistribution matrices for each of the 9 intervals separately.

We fit the data between 100 MeV and 10 GeV using `XSPEC`[62] to test three models. The first two are simple phenomenological functions, to describe bremsstrahlung emission from accelerated electrons, namely a pure power law (PL) and a power law with an exponential cut-off (PLEXP):

$$\frac{dN(E)}{dE} = N_0\, \epsilon^{-\Gamma}\, \exp\left(-\frac{E}{E_{co}}\right); \qquad (1)$$

where Γ is the photon index and E_{co} is the cut-off energy. We found that the data clearly diverge from a pure power law spectrum and that the PLEXP provides a better fit in all time intervals considered. The third model uses templates based on a detailed study of the gamma rays produced from pion decay (Murphy et al. 1987). In this model accelerated high-energy protons (and other ions) with an assumed energy distribution collide with particles of the solar atmosphere, creating π^0 and $\pi^{\pm}$ mesons. A π^0 quickly decays into two gamma-rays, each having an energy of 67.5 MeV in the rest frame of the meson. The decay products of charged $\pi^{\pm}$ mesons (secondary $e^{\pm}$) produce gamma-rays via Bremsstrahlung

[59] We use dead-time corrected count rates from the NaI_2 in the 10–25 keV and 100–300 keV energy bands and from the BGO_0 in the 1–10 MeV energy band.

[60] for `P7SOURCE_V6` class with a cut on the zenith angle, z_{max}=100°

[61] http://apod.nasa.gov/apod/ap120315.html

[62] http://heasarc.gsfc.nasa.gov/docs/xanadu/xspec/index.html

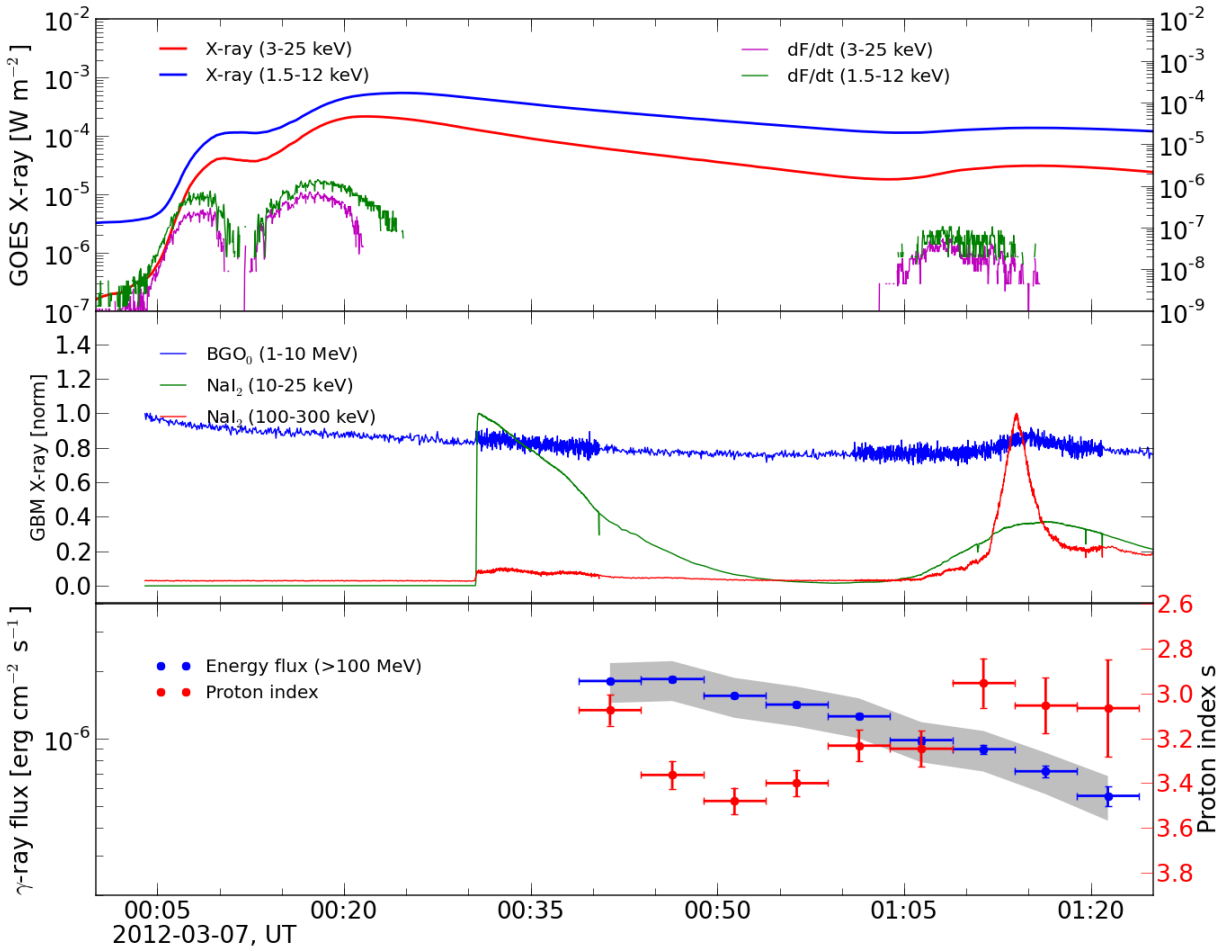

FIG. 1.— Composite light curves for 2012 March 7 flare, covering the first ∼80 minutes. **Top panel**: Soft X-rays (red: 1.5–12 keV, blue: 3–25 keV) from the GOES 15 satellite. On the right axis are the first derivatives of the soft X-rays fluxes (magenta: 1.5–12 keV, green: 3–25 keV). These curves approximate accelerated electron impulsive lightcurves (Neupert 1968). **Middle panel**: Hard X-rays count rates from the GBM; green and red for NaI_2 10–25 keV and 100–300 keV energy channels, and blue for the BGO_0 detector. **Bottom panel**: LAT (>100 MeV) gamma-ray flux (blue) and derived proton spectral index (red). The gray band represents the systematic uncertainties associated to the flux measurement, and it is obtained by adding 20% systematic error in quadrature.

or by annihilation-in-flight of the positrons, and microwaves via synchrotron radiation[63]. The ratio of the $e^{\pm}$ energy going to gamma-rays or to microwaves is $\sim (n/10^{14}\mathrm{cm}^{-3})(1000\mathrm{G}/B)^2(\mathrm{GeV}/E)$. For the magnetic field strength in the solar atmosphere $B = 300$ G used in our templates, synchrotron losses have only a small effect on the transport of the protons to column depths of $> 10^{22}$ cm^{-2} (needed to stop them) or densities of $n > 10^{15}$ cm^{-3}. However, the synchrotron emission may be detectable (see discussion below).

The pion-decay templates used in our fits depends on the ambient density, composition and magnetic field, on the accelerated-particle composition, pitch angle distribution and energy spectrum. The templates represent a particle population with an isotropic pitch angle distribution and a power-law energy spectrum ($dN/dE \propto E^{-s}$, with E the kinetic energy of the protons) interacting in a thick target with a coronal composition (Reames 1995) taking ^{4}He/H = 0.1. To obtain the gamma-ray flux value we fit the data varying the proton spectral index s from 2–6, in steps of 0.1. In this way, we fit the LAT data with a model with two free parameters, the normalization and the proton index, s. The time dependence of the >100 MeV gamma-ray flux and of the proton index, s, derived using gamma-ray LAT data, is displayed in the lower panel of Figure 1 and the numerical values are reported in Table 1, as well as the best-fit parameters of the PLEXP model.

It appears that, after a short phase of spectral softening, the proton spectral index hardens before the start of the impulsive phase of the second flare as seen by the GBM detectors (middle panel of Figure 1). The spec-

[63]The interactions between the accelerated and background protons (and ions) also produce nuclear de-excitation lines in the 1 to 10 MeV range, observable by the GBM. The analysis of these flaring episodes by the GBM will be presented in a subsequent paper.

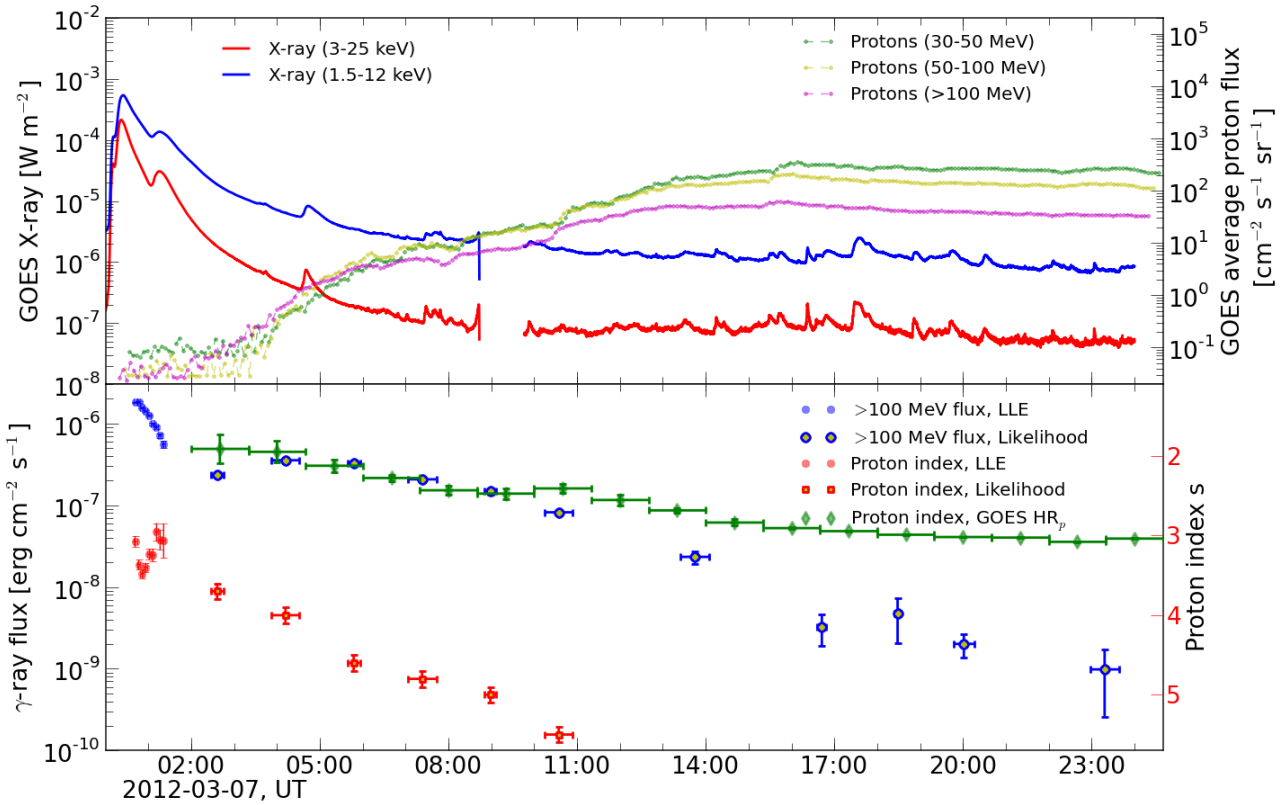

FIG. 2.— Long lasting emission. **Top panel**: soft X-rays (red: 1.5–12 keV, blue: 3–25 keV) from the GOES 15 satellite. On the right axis, 5-minute averaged proton flux (green: 30–50 MeV, yellow: 50–100 MeV, magenta: >100 MeV). We display the average of detectors A and B. **Bottom panel**: high energy gamma ray flux above 100 MeV measured by the *Fermi* LAT. The Blue/red circles represent the flux and the derived proton spectral index obatined with the LLE analysis (covering the initial period, when the instrumental performance was affected by pileup of hard-X-rays in the ACD tiles). Blue/red empty circles/squares represent the flux and the derived proton spectral index obtained by standard likelihood analysis. Green diamonds are the GOES proton spectral indexes derived from the hardness ratio, as described in the text.

tral index s correlates better with the GBM flux than with the high-energy flux measured by the LAT. For the interpretation of these results, see §4.

3.2. *Temporally extended emission*

Following the first 90 m of *Fermi*-LAT observation up to the end of the flaring episode we perform our study using the standard likelihood analysis implemented in the *Fermi*-LAT `ScienceTools`[64] with `P7SOURCE_V6` IRFs, selecting a 12° radius ROI and selecting only photons that arrive at the LAT within 100 degrees of the zenith to reduce contamination from the Earth's limb. We include the azimuthal dependence of the effective area.

To study the temporally extended emission, we perform time resolved spectral analysis in Sun-centered coordinates by transforming the reference system from celestial coordinates to ecliptic Sun-centered coordinates. This is necessary in order to compensate for the effect of the apparent motion of the Sun during the long duration of the flare. We select intervals when the Sun was in the field of view (angular distance from the LAT boresight $< 70°$) and use the unbinned maximum likelihood algorithm `gtlike`. We include the isotropic template model that is used to describe the extragalactic gamma-ray emission and the residual CR contamination (`iso_p7v6source.txt`), leaving its normalization as the free parameter. Over short time scales, the diffuse Galactic emissions produced by cosmic rays interacting with the interstellar medium are not spatially resolved and are hence included in the isotropic template. We also add the gamma-ray emission from the quiescent Sun modeled as a point source located at the center of the disk, with a spectrum described with a simple power-law with a spectral index of 2.11 and an integrated flux (> 100 MeV) of 4.6×10^{-7} ph cm^{-2} s^{-1} (Abdo et al. 2011). We did not include the extended IC component described in Abdo et al. (2011) because it is too faint to be detected during these time scales. We fit the data with the same two phenomenological functions used for the impulsive phase of the flare and use the Likelihood Ratio Test to estimate whether the addition of the exponential cut-off is statistically significant. The Test Statistic TS$= -2\,\Delta\log(\mathcal{L})$ is twice the increment of the logarithm of the likelihood value $\mathcal{L}$ obtained by fitting the data adding the source to the background. Because the null hypothesis is the same for the two cases, the increment of the Test Statistic

[64] We used `ScienceTools` version 09-28-00

TABLE 1
Spectral analysis of the impulsive phase

Time Interval 2012/03/07 UT	Proton index	Energy Flux[a]	Γ	E_{CO} MeV	Flux[a]
00:38:52–00:43:52	3.07±0.07	21±1	−0.07±0.09	130±8	18.0±0.4
00:43:52–00:48:52	3.36±0.07	18.7±0.6	−0.26±0.07	107±4	16.3±0.3
00:48:52–00:53:52	3.48±0.07	15.5±0.3	−0.23±0.06	106±4	14.1±0.2
00:53:52–00:58:52	3.40±0.06	14.4±0.4	−0.19±0.06	109±4	12.7±0.2
00:58:52–01:03:52	3.23±0.07	12.7±0.4	−0.18±0.07	114±5	10.9±0.2
01:03:52–01:08:52	3.25±0.08	9.6±0.3	−0.25±0.08	111±6	8.6±0.2
01:08:52–01:13:52	2.95±0.08	9.0±0.3	0.00±0.05	136±7	7.2±0.2
01:13:52–01:18:52	3.0±0.1	7.2±0.4	0.6±0.10	220±30	6.0±0.3
01:18:52–01:23:52	3.1±0.2	5.7±0.6	0.8±0.20	270±70	5.0±0.5

[a] Integral energy flux between 100 MeV and 10 GeV, in units of 10^{-7} erg cm^{-2} s^{-1}.

(Δ TS=$\mathrm{TS_{PLEXP}}$-$\mathrm{TS_{PL}}$) is equivalent to the corresponding difference of maximum likelihoods computed between the two models.

For each interval, if Δ TS ≥ 50 then the PLEXP model provides a significantly better fit than the simple power-law and we retain the additional spectral component. In these time intervals, we also used the pion decay model to fit the data and estimated the corresponding proton spectral index. We performed a series of fits with the pion decay template models calculated for a range of proton spectral indices. We then fit the resulting profile of the log-likelihood function with a parabola and determine its minimum ($\mathcal{L}_{\rm min}$) and the corresponding value s_0 as the maximum likelihood value of the proton index. The 68% confidence level is evaluated from the intersection of the profile with the horizontal line at $-2\,\Delta\log(\mathcal{L}_{\rm min})+1$. Table 2 summarizes our results. In Figure 3 we compare the observed count spectra with the predicted numbers of counts for the different models. The predicted numbers are the sum of the contribution of the background and of the source, after the spectral parameters are optimized. The contribution of the isotropic background and of the quiescent Sun is also shown in the figures. In the first 6 time intervals (*a* through *f*) a power-law model does not correctly reproduce the data, while a curved spectrum (such as the power law with an exponential cut off or a pion decay model) provides a better description of the data. In the time intervals from g) to j) the power-law representation is sufficient to describe the data; in the last bin, the source is only marginally significant (TS=7).

In the lower panel of Figure 2 we combine the LLE and likelihood analysis results, showing the evolution of both the gamma-ray flux and the derived spectral index of the protons[65]. Unlike during the impulsive phase, the spectrum during the temporally extended phase becomes softer (s increases monotonically). We also compare our results with the GOES proton spectral data. For this, we selected two energy bands (>30 MeV and >100 MeV) and corrected the light curve by the proton time-of-flight (TOF) to 1 AU by considering the TOF for 30 MeV and 100 MeV protons (i.e. the maximum delay in each energy band). As a measure of the spectral index of the SEP protons, we compute the Hardness Ratio HR_p defined as:

$$\mathrm{HR}_p = \log\frac{\mathrm{P}_{>100\mathrm{MeV}}}{\mathrm{P}_{>30\mathrm{MeV}}} \quad (2)$$

[65] After approximately 11:00 UTC the flux of the Sun diminished to the point that the spectral index of the proton distribution cannot be significantly constrained.

from which we calculate the value of the spectral index $s_{\rm SEP}$ of the SEP protons observed at 1 AU that correspond to such HR_p values:

$$s \sim 1 - 0.83\,\mathrm{HR}_p \quad (3)$$

To estimate the uncertainty associated with this procedure we repeat the calculation neglecting the TOF correction. In this way we obtain two values for the SEP spectral index for each time bin, corresponding to the actual and zero delay due to the time of flight. In Figure 2 we report the estimated proton spectral index as the average of these two values and its uncertainty as half the difference of these two values. Note that the values of the proton spectral index inferred from the gamma-ray data are systematically softer than the value of the index derived directly from SEP observation, although the temporal evolution (hard-to-soft) is similar.

In the 6 time intervals within which the pion decay model provides a better fit, we compute the spectral energy distribution by first using the result of the fit with the power law with an exponential cut-off to constrain the background. The normalization of the background is set to the best fit value. We divide the data into 10 energy bins and repeat the spectral analysis in each bin independently. We keep the normalization of the background constant for the bin-by-bin fits and assume that the in-bin spectrum is an E^{-2} power law, with only the normalization allowed to vary. For non-detections (TS<9), we compute 95% CL upper limits. The results are shown in Figure 4. We also report the values of the energy flux in the 6 time intervals in Table 3.

3.3. *Localizing the high energy gamma-rays*

We measure the direction of the > 100 MeV gamma-ray emission using the `gtfindsrc` tool and perform a likelihood analysis on both time-integrated and in separate time intervals. The background is modeled using the best-fit parameters obtained by the time-resolved spectral analysis described in the previous section, and the source is modeled according to the best-fit model. The uncertainties on the localization are obtained by combining the 68% error radius from `gtfindsrc` with the systematic bias associated with the "fisheye" effect in quadrature. We estimate the latter using Monte Carlo simulations and find it to be $0\overset{\circ}{.}02$ ($\approx 70\,''$).

The results for the 6 time bins where the pion template provides the best fit are shown in Figure 5. The localization centroids (with uncertainties) are shown in the

TABLE 2
SPECTRAL ANALYSIS OF THE TIME EXTENDED EMISSION

Interval	Start (UT) 2012/03/07	Duration s	TS_{PL}	ΔTS^a	Γ	E_{co} MeV	Flux^b	Proton index	X,Y ($r_{68} \oplus 70$)^c arcsec
a)	02:27:00	1110	1400	85	-1.1 ± 0.2	260 ± 40	2.3 ± 0.8	3.7 ± 0.1	-280, 140 (320)
b)	03:52:00	2370	16421	982	-0.9 ± 0.1	210 ± 10	3.53 ± 0.09	4.0 ± 0.1	-450, 260 (100)
c)	05:38:32	1050	1393	159	-0.2 ± 0.3	120 ± 10	3.2 ± 0.1	4.6 ± 0.2	-470, 260 (350)
d)	07:03:00	2400	9003	756	-0.4 ± 0.1	130 ± 7	2.08 ± 0.04	4.8 ± 0.1	-500, 130 (150)
e)	08:50:00	1020	500	73	0.2 ± 0.6	90 ± 22	1.5 ± 0.1	5.1 ± 0.3	670, 580 (750)
f)	10:14:32	2370	1833	204	0.3 ± 0.2	80 ± 9	0.81 ± 0.03	5.5 ± 0.2	440, 380 (330)
g)	13:25:00	2400	137	13	0.05 ± 1.0	80 ± 30	0.24 ± 0.04	–	–
h)	16:36:00	780	17	8	1.0 ± 0.1	50 ± 10	0.03 ± 0.01	–	–
i)	18:24:00	540	10	3	1.0 ± 0.1	33 ± 9	0.05 ± 0.03	–	–
j)	19:47:00	1710	59	2	-1.5 ± 0.8	350 ± 300	0.02 ± 0.01	–	–
k)	22:58:30	2370	7	4	1.0 ± 0.1	230 ± 70	0.010 ± 0.007	–	–

[a] $\Delta TS = TS_{PLEXP} - TS_{PL}$.
[b] Energy Flux of gamma-rays between 100 MeV and 10 GeV, in units of 10^{-7} erg cm^{-2} s^{-1}, calculated using the best fit model.
[c] A systematic error of 70 arcsec has been added in quadrature to the estimated 68% error radius, and is reported between parenthesis.

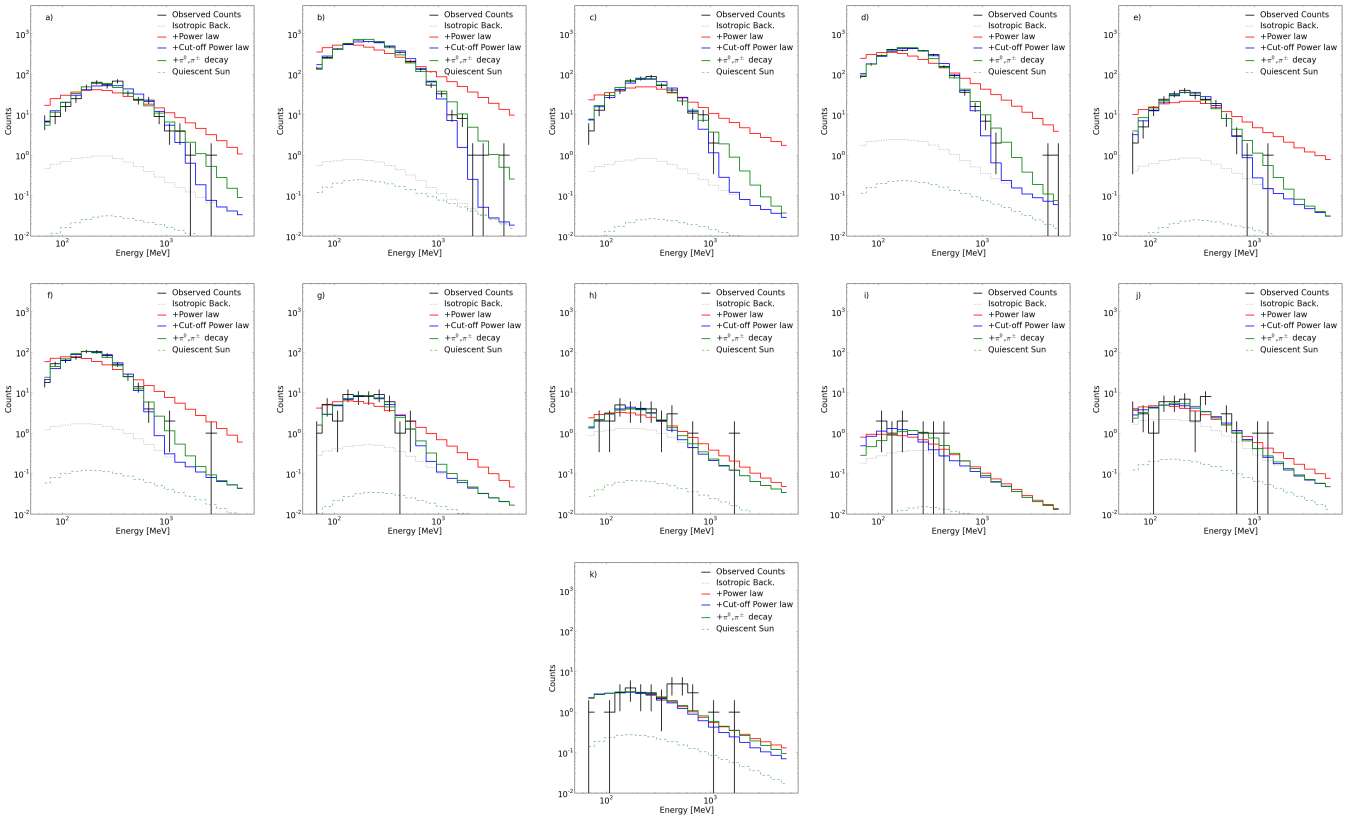

FIG. 3.— Comparison between observed counts (black thick line) and model predictions. The dotted black line is the isotropic background (sum of the Galactic and isotropic background), the green dashed line is the contribution from the quiescent Sun. The red, green and blue thick lines are the predicted numbers of counts from background + source modeling the solar flare with a power law, a power law with exponential cut-off, and with a pion decay model, respectively. Statistical uncertainties are associated to the numbers of observed counts using the Gehrels (1986) prescription for confidence level in the low counts regime. These errors are not considered in the likelihood fit (which only compare the number of observed events with the number of predicted events assuming Poisson statistics) but are useful to visualize the statistical uncertainty due to Poisson fluctuation in each bin. The time intervals are defined in Table 3.

last column of Table 1. For the remaining time intervals, the reconstructed location of the emission is consistent with the direction of the Sun, although the associated uncertainty is larger than the angular diameter of the Sun.

During the $\sim$ 20 hours of detected flaring gamma-ray emission, the LAT measured 5 photons with E > 2.5 GeV and reconstructed direction less than 1° from the center of the solar disk. All 5 of these events belong to the `P7SOURCE_V6` event classe and 3 of them are also `P7ULTRACLEAN_V6`. Two of these photons, with energies 2.8 GeV and 4 GeV, were detected during the impulsive phase of the flare and the remaining three during the extended emission, including one with E=4.5 GeV

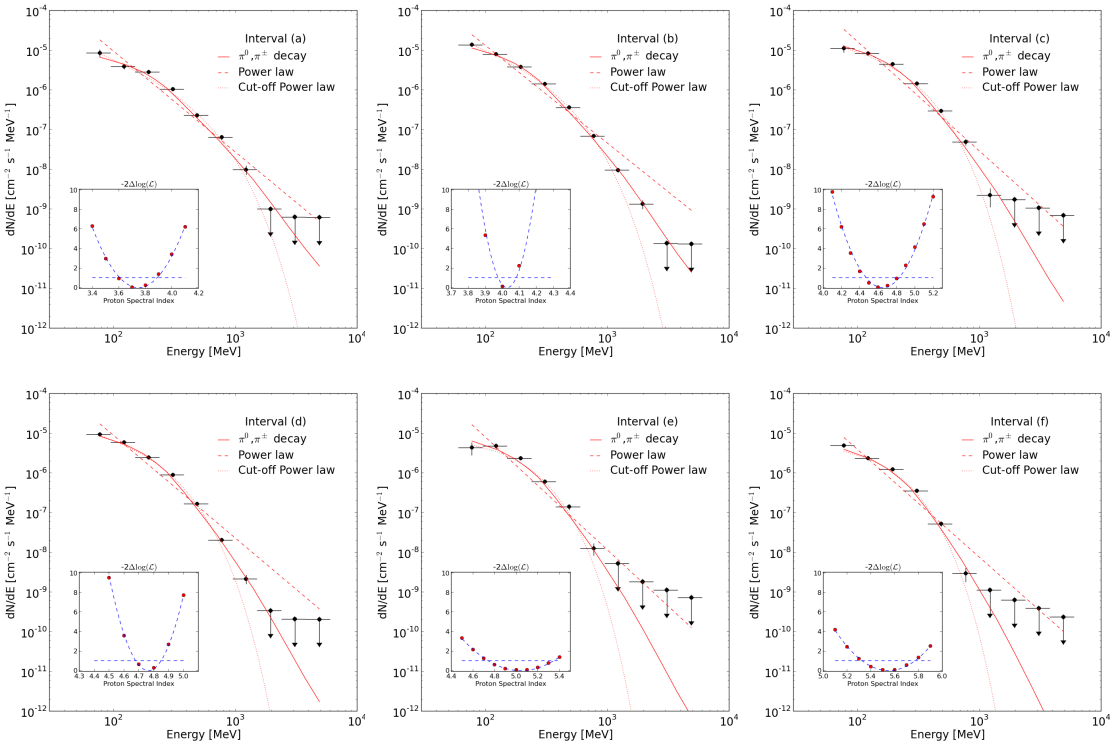

FIG. 4.— Spectral energy distribution in the 6 time intervals for which the pion decay model provided the best fit to the data. For each time interval we illustrate the models used for fitting the broad band spectrum: power law (dashed), power law with an exponential cutoff (dotted) and pion decay template model (solid). In the insets we report the profile of the likelihood function -2$\Delta\log(\mathcal{L})$ which is used to estimate the pion template model that best match the data. The scans are performed as functions of the index of the proton distribution used to compute the templates. The intersections with the horizontal dashed lines represent the 68% confidence levels used to estimate the errors.

TABLE 3
SPECTRAL ENERGY DISTRIBUTION

Energy Bin MeV	Energy Flux $\times10^{-9}$ erg cm^{-2} s^{-1}					
	a)	b)	c)	d)	e)	f)
60–95	64±17	117±6	83±21	79±5	31±14	40±5
95–150	79±13	175±6	171±21	129±5	96±16	49±4
150–239	149±14	211±6	236±19	134±5	121.1±14	65±4
239–378	137±13	198±6	190±16	123±5	76.2±11	46±4
378–600	73±10	123±5	94±12	56±4	41.8±8	16±3
600–950	49±8	57±4.2	36±8	16±2	7.5±4	< 4
952–1508	16±6	19±3	< 12	3±1	< 12	< 2
1509–2391	< 14	6±2	< 10	< 2	< 10	< 4
2391–3789	< 21	< 5	< 15	< 3	< 16	< 6
3780–6000	< 22	< 5	< 25	< 7	< 26	< 8

at 07:30UT. Comparing the distance from the center of the solar disk and the predicted 68% containment radius from the point spread function (PSF) of the instrument we find that four of the events are consistent with the solar disk. In the case of the 4.5 GeV photon, the reconstructed direction is 0.°8 from the center of the solar disk and the 68% containment radius is approximately 0.°2. Therefore we conclude that the reconstructed direction of this event is only marginally consistent with the solar disk.

Considering the average rate of LAT detected photons above $\sim$ 2.5 GeV coming from an ROI with radius 1° centered at the Sun (calculated using all available flight data, excluding the bright LAT detected solar flare time intervals) we find that the probability to observe five or more events in 8 hours due to Poisson fluctuations is approximately P=8.0$\times10^{-6}$ ($\sim$ 4.8σ). In Table 4 we list some of the basic properties of these photons, including the arrival time, energy, reconstructed distance from the center of the solar disk, reconstructed direction with respect to the instrument coordinate system, 68% containment radius and conversion type.

4. DISCUSSION AND INTERPRETATION

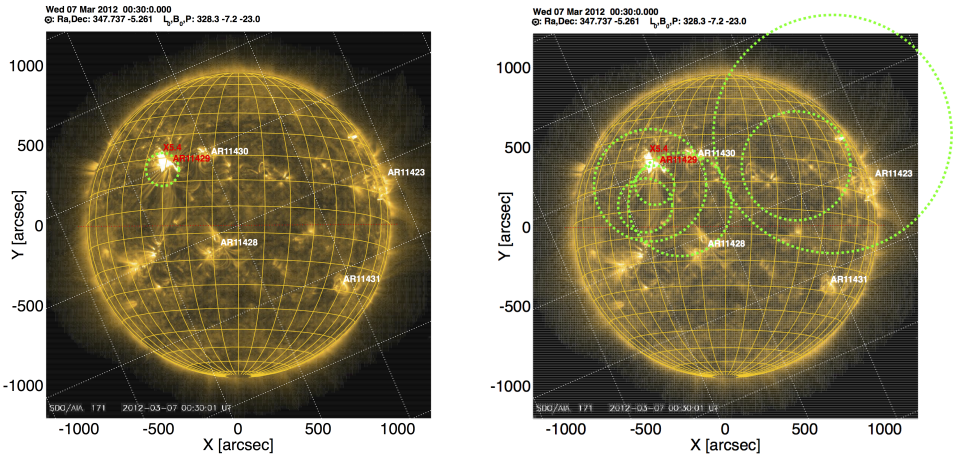

FIG. 5.— Location of the gamma ray emission above 100 MeV for the time-integrated (left) and the time resolved (right) analysis. The images on the background are from SDO (AIA 171Å) and are taken at the time of the flaring episode. Active regions are flagged with their respective NOAA numbers. The region associated with the X-class flares is indicated with a red label, located at N16E30 (X,Y=-471,373″). The green circles are the 68% source location uncertainty regions (+systematic error added in quadrature). The grid on the background is the coordinate grid of equatorial coordinates, while the yellow sphere is the heliocentric coordinate grid (with the projected solar rotation axis parallel to the Y-axis, the Z-axis is the line of sight (from the Sun to the observer) and the X-axis in the cartesian projection complete the normal basis.

TABLE 4
HIGH ENERGY EVENTS

Arrival Time 2012/03/07 UT	Energy GeV	Distance (deg)	θ (deg)	Event Class	Conversion	$PSF^a_{68\%}$ (deg)
0:49	2.8	0.2	49	SOURCE	FRONT	0.3
1:18	4	0.6	66	ULTRACLEAN	BACK	0.5
2:35	2.9	0.6	62	SOURCE	BACK	0.6
4:12	2.9	0.5	36	ULTRACLEAN	BACK	0.6
7:30	4.5	0.8	44	ULTRACLEAN	FRONT	0.2

[a] $PSF_{68\%}$ corresponds to the 68% containment radius calculated from the PSF of the instrument for an energy and direction equal to the energy and direction of the event.

The sensitivity of the *Fermi*-LAT enables the investigation of several aspects of solar flares that were not previously accessible, in particular the spectral evolution during the impulsive phase and throughout the temporally extended phase, as well as the localization of the > 100 MeV emission. The data for the exceptionally bright solar flares of 2012 March 7 represent an excellent opportunity to study the details of these characteristics. Here we focus on the possibility of constraining the emission and acceleration processes.

For the initial four time intervals the projected location of the gamma-ray emission is consistent with the position of the active region #11429. While in the last two time intervals the localizations are slightly displaced with respect to this region, but still consistent with the solar disk.

GOES fluxes began to rise at about 00:05:00 UT, and continued to increase for over an hour, while *Fermi* sunrise started roughly six minutes after the peak of the first flare at 00:30:00 UT. This coincided with the gradual decay phase during which the hard X-ray (HXR) emission is relatively soft. The GBM detected only weak emission above 100 keV during the first flare. On the other hand, the second flare had a large flux in the 100-300 keV range and a significant flux above 1 MeV, which indicates acceleration of electrons up to several MeVs. The derivative of the GOES flux has a pulse shape with a similar structure to that of the lowest energy GBM channel. These pulses show the usual soft-hard-soft spectral evolution in the HXR regime. However, the LAT > 100 MeV emission has a monotonically decreasing flux that is approximately exponential with a ~ 30 m decay period. There is no significant evidence for an upturn in flux during the X1.3 flare, while the derived proton index does show some variation. The pion-decay model, which fits well, requires a relatively hard proton spectrum with the power-law index, s, ranging between $\sim$3.0 and $\sim$3.5. The spectrum is initially soft, but then exhibits evidence of spectral hardening during the second flare, as also appears to be the case in the HXR regime (Figure 1). The hardening seems to start $\sim$20 minutes before the start of the X1.3 flare. However, the significance of this early hardening is less than 3σ. If this is real, explanations for spectral hardening during the decay phase can be an intensification of the acceleration rate or, alternatively, to trapping of accelerated particles in a coronal loop with a converging magnetic field configuration (see below).

The temporally extended emission is characterized by a slight increase of the gamma ray flux starting at approximately 2:15:00 UT; the flux reaches its maximum at

approximately 4:00:00 UT. The peak of the light curve is broad and the flux after t_0=12:00 UT decays exponentially as $F(t) \propto \exp[-(\mathrm{t}-\mathrm{t}_0)/\tau]$, with an exponential decay period $\tau \approx 2.7$ hours. The gamma ray spectrum and thus the required particle spectrum softens monotonically during the first six time intervals, with no sign of an early rise or a plateau as seen in the flux. The hardness ratio of the SEP protons also shows similar softening except there seems to be some deviation at about 10:00 UT which could be due to subsequent events (e.g. the GOES event before 05:00 UT). The SEP proton spectrum is much harder, with index smaller by 2–3 units, than the spectrum of the protons making the gamma rays, as seen in the bottom panel of Figure 2.

We now describe to what extent these new observations constrain the models. In particular, we discuss continuous versus prompt acceleration in a magnetic trap, proton versus electron emission, and proton versus electron emission and acceleration at the coronal reconnection site versus CME shock.

4.1. *Prompt vs Continuous Acceleration*

In the prompt acceleration model particles are injected quickly, e.g., as a power-law spectrum, into a trap region where they gradually lose energy and emit radiation (Murphy et al. 1987; Kanbach et al. 1993b). If the radiation is produced in the trap region then we expect a spectral variation that depends on the energy dependence of the energy loss rate (Aschwanden 2004). For relativistic electrons moving in a medium with particle density n and magnetic field $B_{\rm eff}$, the energy-loss rate is given by:

$$\dot{E}_L(E) = \frac{E_p}{\tau_0}\left[1+\left(\frac{E}{E_p}\right)^2\right] \qquad (4)$$

where $\tau_0 \sim 10^4\,(10^{10}\mathrm{cm}^{-3}/n)$ s and $E_p \sim 10\,\mathrm{MeV}\,(n/10^{10}\mathrm{cm}^{-3})^{1/2}(100\mathrm{G}/B_{\rm eff})$. This produces characteristic spectra that are flat at low energies ($E < E_p$: due to Coulomb energy losses) and have a sharp cut off at high energies ($E > E_p$: due to synchrotron and Inverse Compton (IC) losses) in less than an hour (see e.g. Petrosian 2001)[66]. This clearly disagrees with the data that indicate a power-law spectrum at low energies with a gradual energy cut off. For $0.1-10$ GeV protons the timescale for the energy loss (due to Coulomb losses), τ_L=$(E/\dot{E}_L) \sim 6\times10^3\,(10^{10}\mathrm{cm}^{-3}/n)(E/0.1\,\mathrm{GeV})^{1.5}$ s and is almost constant $\sim 2\times10^5$ s above 10 GeV (p–p interactions). This causes a hardening of the spectra (index decreasing by 1.5) within several hours, which also disagrees with the observed spectral evolution. The marginally significant hardening within a few minutes before the X1.5 flare requires a density of $n \gg 10^{10}$ cm^{-3}, which is not appropriate for a coronal trap model (Ryan 1986).

An alternative scenario is the trap precipitation model (Bai 1982) where the trapped particles are scattered into the loss cone that causes their precipitation into the chromosphere and below, where they lose most of their energy and produce gamma rays. Coulomb collisions cannot be the agent for this scattering, because the relativistic electron Coulomb scattering rate is lower than the Coulomb energy loss rate by a factor of γ^2 and is much smaller than synchrotron energy loss or IC scattering rate. In addition, the Coulomb scattering rate for protons is lower than the energy loss rate for electrons by a factor proportional to the electron to proton mass ratio. In other words, with Coulomb scattering the particles lose energy before they are scattered into the loss cone. Therefore, a much faster scattering rate is required for this scenario. Scattering by turbulence could be a possibility but in that case acceleration by turbulence will also be present so we no longer have a prompt model. Thus, we conclude that a more likely scenario is continuous acceleration (e.g. by turbulence; see Petrosian & Liu 2004) with a timescale comparable to, or shorter than, the particle energy-loss timescale.

[66]Note that even for $B=0$ the IC losses in the optical photon field of the Sun, with effective field of 10 G, makes the energy loss timescale for IC scattering less than a day but not as short as synchrotron losses.

4.2. *Electron vs proton emission*

For electrons, non-thermal bremsstrahlung is the only viable mechanism of gamma-ray production (Trottet & Vilmer 1984; Vilmer 1987). However, there are some important caveats. The first is that for >100 MeV electrons bremsstrahlung is inefficient. The bremmstrahlung emission time scale $\tau_{\rm brem} \sim 3\times10^4(10^{10}\mathrm{cm}^{-3}/n)(\mathrm{GeV/E})^{0.1}$ s is much longer than the synchrotron energy-loss time $\tau_{\rm sync} \sim 40\,(\mathrm{GeV/E})(100\mathrm{G}/B)^2$ s and even the IC scattering energy-loss time scale $\tau_{\rm IC} \sim 8\times10^3(\mathrm{GeV}/E)$ s. Thus, a much larger microwave and HXR flux would be expected; whether there are observations that can rule out this possibility is unknown to us. In addition, the highest energy photon observed by the *Fermi*-LAT of 4 GeV would require electrons to be accelerated to about 10 GeV. This implies acceleration timescales of less than a few seconds over a period of a day to overcome the aforementioned synchrotron losses. Therefore, protons seem to be more likely agents of the gamma ray production and a power-law spectrum for these particles seems to agree fairly well with the data. As mentioned above, protons with energies less than 10 GeV lose energy predominately via Coulomb collisions with the background electrons with a time scale τ_L that is constant to $>\sim 50$ hours above several GeV. This indicates that the emission originates from regions with densities much higher than those found in the upper corona. This implies thick target emission by protons directed toward the chromosphere that, for a continuous injection spectrum $\dot{Q}(E)$, implies an effective thick target proton spectrum:

$$N_{\rm eff}(E) = \left[\frac{\tau_L(E)}{E}\right]\int_E^\infty dE'\;\dot{Q}(E'). \qquad (5)$$

Thus, for an injected power-law $\dot{Q}(E) \propto e^{-\delta}$ the effective spectrum will be a broken power-law steepening with an index change from 1 to 1.5 around several GeV. Whether a spectrum more complicated than a power law can describe the observations adequately is beyond the scope of the current paper. It should also be noted that the yield of gamma-rays is about 1% at the pion production threshold of ~ 300 MeV but becomes essentially 50% above a few GeV (the other half of the proton energy going to neutrinos).

From the results of the gamma-ray spectral analysis, and using the gamma-ray yield in Murphy et al. (1987), we estimate the number and energy of the accelerated protons with kinetic energy >30 MeV producing gamma-rays and observed as SEPs. During the first impulsive phase the estimated number (energy) of protons interacting with the Sun is $N_p \sim 2.5\times10^{33}$ ($\mathcal{E}_p \sim 2.2\times10^{29}$ erg), while, for the temporally extended emission, is approximately $N_p \sim 1.0\times10^{34}$ ($\mathcal{E}_p \sim 6.9\times10^{29}$ erg). From the GOES observations, we estimate that the number (energy) of SEP protons escaping the CME shock during the period of time when the gamma-ray flux was high (until March 8) is $N_{SEP} \sim 4.0\times10^{34}$ ($\mathcal{E}_{SEP} \sim 4.2\times10^{30}$ erg) or, for the full period of time when the proton flux was high (i.e. until approximately 20:00 UT of March 12) is $N_{SEP} \sim 1.37\times10^{35}$ ($\mathcal{E}_{SEP} \sim 1.23\times10^{31}$ erg)[67]. We conclude that protons producing gamma-rays carry significantly less energy than SEP protons observed by GOES.

4.3. *Acceleration at the Corona vs CME Shock*

Continuous acceleration of protons at the flare reconnection region, whether by stochastic acceleration mechanism (Petrosian & Liu 2004) or by a standing shock can account for most of the spectral observations described above. In this model protons escape the acceleration site along closed field lines into the chromosphere and the spectral changes are simply due to the softening of the spectrum as the flare decays. In stochastic acceleration by turbulence the accelerated particle spectra become softer as the turbulence weakens, which can naturally explain such a spectral evolution. Acceleration at the CME shock (Rank et al. 2001) is also an attractive explanation because the SEP protons, which are most likely accelerated at the shock and escape in the upstream direction (Ramaty et al. 1990), show the same kind of spectral evolution. However, these spectra are much harder and have a spectral index similar to the impulsive phase index deduced for protons producing the gamma-rays. In addition, gamma-ray production can occur only in the high-density chromosphere so that CME protons must escape downstream into the highly turbulent region behind the shock and be transported back to the Sun against a high-speed outflow. The Large Angle and Spectrometric Coronagraph (LASCO, Brueckner et al. 1995) on board the solar and Heliospheric Observatory (SOHO) mission, observed a fast CME ejected at approximately 00:30 UT, and measured the speed and acceleration of the head of the fastest segment of the leading edge (Gopalswamy et al. 2009). The average speed was approximately 2684 km s^{-1}, while the acceleration obtained by fitting the height (vs. time) of the leading edge was ≈ -88 m s^{-2}. The last available measurement indicates that the speed of the CME at 1 solar radius from the photosphere was $\approx$2379 km s^{-1}. Using this information, we estimated that in 10 hours, the CME would have traveled approximately 80 $R_\odot$(0.36 AU), requiring the protons accelerated by the CME shock front to travel back along the magnetic lines connected to the Sun for very large distances. In this scenario, it is possible that the current sheath (CS) provided a preferred path magnetically connecting the front of the CME shock with the original flare site. The displacement of the reconstructed position at later times can be explained by larger dispersion of particles due to the longer distance traveled. This model provides the correct scenario for short acceleration time scales ($\sim$1 hr). If continuous acceleration happens at the flare site, as suggested by Petrosian & Liu (2004), low-energy protons accelerated at the Sun (vastly larger in number than high-energy protons) can escape along open field lines, reach the CME, and be re-accelerated as SEPs by the shock front. This would explain the observed correlation between the gamma-rays and SEP spectral properties.

Finally, it should be noted that we expect electrons to be accelerated as well. Exactly how much energy goes to protons and how much to electrons depends on the acceleration mechanism. As shown in Petrosian & Liu (2004) generally more energy goes to electrons in more strongly magnetized plasmas like those existing in the solar corona. How many electrons will be accelerated and what their radiative signature will be is beyond the scope of this paper. However, we note that Nobeyama (Nakajima et al. 1995) radio data at both 17 GHz and 34 GHz show a bright signal starting on March 6 at approximately 22:45 UT, reaching its maximum on March 7 at 01:13, and ending at approximately 03:02 UT. No sign of radio activity is visible at later times, suggesting that highly energetic electrons might explain part of the >100 MeV gamma-ray emission only at earlier times, whereas the temporally extended emission is likely to be attributed to energetic protons (and ions).

In summary, in this paper we have presented the analysis of the brightest solar flare detected by the *Fermi* LAT to date. We have shown that during most of the long duration emission the gamma-rays appear to come from the same active regions responsible for the flare emission. The fluxes and spectra of the high-energy gamma-rays evolve differently during the impulsive phase and the sustained emission. Also there are correlations and some differences between the fluxes and spectral indexes of the protons required for the production of high-energy gamma-rays and SEP protons seen at 1 AU. From these data we suggest that the most likely scenario for production of high energy gamma-rays is that they are produced by energetic protons (rather than electrons) that are accelerated in the corona (rather than in the associated fast CME shock) continuously during the whole duration of the emission.

The *Fermi* LAT Collaboration acknowledges generous ongoing support from a number of agencies and institutes that have supported both the development and the operation of the LAT as well as scientific data analysis. These include the National Aeronautics and Space Administration and the Department of Energy in the United States, the Commissariat à l'Energie Atomique and the Centre National de la Recherche Scientifique / Institut National de Physique Nucléaire et de Physique des Particules in France, the Agenzia Spaziale Italiana and the Istituto Nazionale di Fisica Nucleare in Italy, the Ministry of Education, Culture, Sports, Science and Technology (MEXT), High Energy Accelerator Research Organization (KEK) and Japan Aerospace Exploration Agency (JAXA) in Japan, and the K. A. Wallenberg Foundation,

[67]The relative values for protons at other energies will differ from the above numbers because of the differences in indexes.

the Swedish Research Council and the Swedish National Space Board in Sweden.
Additional support for science analysis during the operations phase is gratefully acknowledged from the Istituto Nazionale di Astrofisica in Italy and the Centre National d'Études Spatiales in France.

We also wish to acknowledge G. Share for his continuous support and important contribution to the *Fermi* LAT collaboration.

APPENDIX

THE LAT LOW ENERGY ANALYSIS

The LAT Low energy (LLE) technique is an analysis method designed to study bright transient phenomena, such as GRBs and solar flares, in the 30 MeV–1 GeV energy range. The LAT collaboration (Atwood et al. 2009) developed this analysis using a different approach than the one used in the standard photon analysis which is based on sophisticated classification procedures (a detailed description of the standard analysis can be found in Atwood et al. 2009; Ackermann et al. 2012b). The idea behind LLE is to maximize the effective area below ~ 1 GeV by relaxing the standard analysis requirement on background rejection. The basic LLE selection is based on a few simple requirements on the event topology in the three subdetectors of the LAT namely: a tracker/converter (TKR) composed of 18 x–y silicon strip detector planes interleaved with tungsten foils; an 8.6 radiation length imaging calorimeter (CAL) made with CsI(Tl) scintillation crystals; and an Anticoincidence Detector (ACD) composed of 89 plastic scintillator tiles that surrounds the TKR and serves to reject the cosmic-ray background.

First of all, an event passing the LLE selection must have at least one reconstructed track in the TKR and therefore an estimate of the direction of the incoming photon. Secondly, we require that the reconstructed energy of the event be nonzero. The trigger and data acquisition system of the LAT is programmed to select the most likely gamma-ray candidate events to telemeter to the ground. The onboard trigger collects information from all three subsystems and, if certain conditions are satisfied, the entire LAT is read out and the event is sent to the ground. We use the information provided by the onboard trigger in LLE to efficiently select events which are gamma-ray-like. In order to reduce the amount of photons originating from the Earth limb in our LLE sample we also include a cut on the reconstructed event zenith angle (i.e. angle $<90°$). Finally we explicitly include in the selection a cut on the region of interest, i.e. the position in the sky of the transient source we are observing. In other words, the localization of the source is embedded in the event selection and therefore for a given analysis the LLE data are tailored to a particular location in the sky.

LLE response files

The LLE response files are generated based on dedicated Monte Carlo simulations. The simulations are used to study how the detector is "illuminated" by a source of a known flux and known position, during the real pointing history of the LAT. We do this by simulating a bright point source with a spectrum $dN/dE \sim E^{-1}$ at the position of the source in question (the Sun in this case), and using the pointing information saved in the spacecraft data file (`FT2` file). We use the Fermi-LAT full simulator (Baldini et al. 2006) to generate particles from the point source, incident over a cross-sectional area of 6 m^2, which illuminates the entire LAT. The LAT detector is represented by a complex model containing more than 34000 volumes. Gamma-ray conversion and particle propagation through the detector is implemented using `GEANT4` (Geant4 Collaboration et al. 2003) while digitization and reconstruction are done using the same algorithm used for flight data. We then apply the LLE selection and bin the resulting events in reconstructed energy versus Monte Carlo energy (`McEnergy`) obtaining the so-called Redistribution Matrix, R_{ij}. This matrix is proportional to the probability that an incoming photon of energy $E \in [E_j, E_{j+1}]$ will be detected in the reconstructed energy bin $[E_i, E_{i+1}]$. We re-normalize each bin such that:

$$\sum_i R_{ij} = A_j = 6 \times 10^4 \mathrm{cm}^2 \frac{N_j(E_{j+1} - E_j)}{N_{\mathrm{TOT}}(E_{MAX} - E_{MIN})}, \tag{A1}$$

where N_{TOT} is the total number of simulated events over an area of 6 m^2 (typically 10^7), N_j is the number of detected events (that survive the selection cuts) with a `McEnergy` between E_j and E_{j+1}. A_j is usually defined as the effective collecting area of the instrument. The Redistribution Matrix File (RMF) is saved in the standard `HEASARC RMF` File Format[68]

Orbital background subtraction

In the case of short and bright transient gamma-ray sources, it is possible to select time windows before and after the transients (the "off-pulse" region) and, excluding the time window of the transient itself, fit the count rates in the off-pulse region with a polynomial function and in this way estimate, the background in the time interval of the transient. For LLE data, this analysis is described in Pelassa et al. (2010) and was applied to the June 12 2010 flare, as presented in Ackermann et al. (2012a). This approach relies on a few assumptions: the background should not vary too much during the transient emission and also the amount of statistics should be sufficient to constrain the fit. These assumptions usually are satisfied when the interval of the transient emission is shorter than the *Fermi* orbital period (≈ 90 minutes).

[68] Described here: `http://heasarc.gsfc.nasa.gov/docs/heasarc/caldb/docs/memos/cal_gen_92_002/cal_gen_92_002.html#Sec:RMF-format`.

For the 2012 March 7 flare presented here, the standard LLE approach to estimate the background by fitting the intervals before and after the flare could not be used because the flaring episode lasted longer than the orbital period. Instead, we estimate the background using data acquired in other orbits. *Fermi* passes through approximately the same geomagnetic configuration every 15 orbits, but given the standard rocking profile (alternating one orbit north and one orbit south) only the 30th orbit approximates similar geomagnetic and pointing conditions, and consequently a similar background rate. We do not average multiples of 30 orbits because they become less reliable, as they span observations further removed in time. This method of background estimation has been used for a number of background-dominated instruments in solar flare analyses, including historically for SMM-GRS (Vestrand et al. 1987; Murphy et al. 1990) and EGRET Kanbach et al. (1993a)[69] and currently for Fermi GBM (Fitzpatrick et al. 2011).

The background files produced for each interval are saved as standard `PHA-I`[70] files. We used `XSPEC` to execute a forward-folding fit, where the model $M(p_1, p_2, ...)$ is folded with the redistribution matrix,R_{ij}, and the results are compared with the background-subtracted signal S_i:

$$S_i = C_i - B_i \stackrel{?}{=} \sum_j R_{ij} M_j(p_1, p_2, ...); \tag{A2}$$

where $M_j(p_1, p_2, ...)$ is the expected number of events between E_j and E_{j+1} for the time interval being analyzed. A maximum likelihood algorithm is then used to calculate the set of parameters that best model the data (see the `XSPEC` manual for details.)

Validation and systematic uncertainties

A detailed paper on the assessment of the systematic errors is in preparation; here we summarize the main results. Generally speaking, discrepancies between the actual response of the LAT and the response matrix derived from simulations can cause systematic errors in spectral fitting. We investigated the systematic uncertainties tied to the LLE selection by following the procedure described in Abdo et al. (2009b). In particular, we compared Monte Carlo with flight data, using the Vela pulsar (PSR J0835–4510) as a calibration source. The pulsed nature of the gamma-ray emission from this source (Thompson et al. 1975) gives us an independent control on the residual charged particle background. In fact, off-pulse gamma-ray emission is almost entirely absent, and a sample of "pure photons" can be simply extracted from the on-pulse region, after the off-pulse background is subtracted. Considering all time intervals during which the Vela pulsar was observed at an incidence angle θ<80°, we estimate the discrepancy between the efficiency of the selection criteria in the LAT data and in Monte Carlo to be ∼17% below 100 MeV, decreasing down ∼8% at higher energies, with an average value ∼9% (note that this average is weighted by the Vela spectrum).

Additionally, we performed a spectral analysis of the Vela pulsar, comparing LLE results with standard likelihood analysis. The >100 MeV flux obtained from the LLE analysis is 20% lower than published in Abdo et al. (2009a) and 16% less than the flux reported by Abdo et al. (2010). In our analysis of the impulsive phase of the 2012 March 7 flare we added a conservative 20% systematic error in quadrature (represented by the grey band in Figure 1).

Finally, we also studied the energy resolution using large samples of simulated events with the Fermi-LAT full simulator. No significant bias was found, and the energy resolution for LLE is estimated to be ∼ 40% at 30 MeV, ∼30% at 100 MeV and < 15% above.

File Format and Availability

LLE data are generated for each burst (GRB or solar flare) that trigger the GBM. We first bin the data in energy and time, and, following the procedure described in (Fermi-LAT Collaboration 2013), we select the background region by selecting all the LLE events before the trigger and after 300 seconds from the trigger. We fit each energy bin with a polynomial function of the cosine of the source bore-sight angle as a function of time and we interpolate the background fit into the signal region. We evaluate statistical fluctuation of the signal above the expected background. This procedure is optimized taking into account different signal region and different time binning. We finally look at the post trial probability. Every detected signal with a post trial probability greater than 4σ is promptly made available through the `HEASARC` web site[71]. For each such detected GRB or solar flare, six different files are delivered:

1. The `LLE event file` format is similar to the LAT photon file format with some exceptions. Because the LLE data are tightly connected to a particular object (position and time), the `FITS` keyword `OBJECT` has been added to the file. Generally, `OBJECT` will correspond to the entry of the GBM Trigger Catalog[72] used to generate LLE data and corresponds to the "name" column in the `FERMILLE` table (and in the GBM Trigger Catalog table). The direction of the source used for selecting the data for the LLE file is also written in the header of each extension of each LLE file. `PROC_VER` corresponds to the iteration of the analysis of LLE data. `PASS_VER` corresponds to the iteration for the reconstruction and the general event classification (Pass6, Pass7, etc.). `VERSION` corresponds to the version of the LLE product for the particular GRB or solar flare represented in the file.

2. The `CSPEC` file is obtained from directly binning the LLE event files. It provides a series of spectra, accumulated with 1 s binning (typically from −1000 to 1000 s around the burst). Each spectrum is binned in 50 energy channels, ranging typically from 10 MeV to 100 GeV. The format of the `CSPEC` file is tailored to satisfy `rmfit`[73]

[69] In Kanbach et al. (1993a) an average for ±N×16 orbits (for N=1,2,3) was used.
[70] `http://heasarc.gsfc.nasa.gov/docs/heasarc/ofwg/docs/spectra/ogip_92_007/node5.html`
[71] FERMILLE, at `http://heasarc.gsfc.nasa.gov/W3Browse/fermi/fermille.html`
[72] `http://heasarc.gsfc.nasa.gov/W3Browse/fermi/fermigtrig.html`
[73] `http://fermi.gsfc.nasa.gov/ssc/data/analysis/user/`

standards, and it is not directly usable in `XSPEC`.

3. The `CSPEC Response` file (the RSP file) is the detector response matrix calculated from Monte Carlo simulation, and it corresponds to a single response matrix for each GRB or solar flare.

4. The `PHA-I`file contains the count spectrum. The `PHA-I` file is created from the same time interval used to compute the response matrix.

5. The selected events file is identical to the LLE event file with an additional selection on time interval applied to match the selection used to compute the response matrix and `PHA-I` files.

6. The LAT pointing and livetime history file is identical to the standard LAT file but with entries every s (instead of every 30 s). It typically spans the range ±4600 s from the trigger time.

The complete LLE selection used to select the events is saved in the keyword `LLECUT` in the primary header of each LLE file. If the GBM catalog position of the burst is updated (due to a refined localization from the LAT or Swift or from subsequent on-ground analysis), the LLE data are automatically updated and new versions of the LLE files are produced. In some cases, LLE data are manually generated (using a better localization which may or may not have been used in the GBM Trigger Catalog). If the direction of a GRB is revised based on follow-up observations with other instruments, regenerated LLE files will have the `VERSION` number incremented, but will leave the `PASS_VER` and `PROC_VER` unchanged.

In general we do not deliver the background estimates for the time ranges around the burst triggers, and we let the user estimate the background using the procedure described in Pelassa et al. (2010). For the reason explained above, we cannot perform this analysis on the 2012 March 7 flare. Therefore, for this particular flare, we provided LLE data including background files.

REFERENCES

Abdo, A. A., et al. 2009a, ApJ, 696, 1084
—. 2009b, Astroparticle Physics, 32, 193
—. 2010, ApJ, submitted
Abdo, A. A., Ackermann, M., Ajello, M., et al. 2011, ApJ, 734, 116
Ackermann, M., Ajello, M., Allafort, A., et al. 2012a, ApJ, 745, 144
Ackermann, M., Ajello, M., Albert, A., et al. 2012b, ApJS, 203, 4
Aschwanden, M. J. 2004, Physics of the Solar Corona. An Introduction, ed. Aschwanden, M. J. (Praxis Publishing Ltd)
Atwood, W. B.Abdo, A. A., Ackermann, M., Ajello, M., et al. 2009, ApJ, 697, 1071
Bai, T. 1982, in American Institute of Physics Conference Series, Vol. 77, Gamma Ray Transients and Related Astrophysical Phenomena, ed. R. E. Lingenfelter, H. S. Hudson, & D. M. Worrall, 409–417
Baldini, L., Bastieri, D., Boinee, P., et al. 2006, Nuclear Physics B Proceedings Supplements, 150, 62
Brueckner, G. E., Howard, R. A., Koomen, M. J., et al. 1995, Sol. Phys., 162, 357
Esposito, J. A., Bertsch, D. L., Chen, A. W., et al. 1999, ApJS, 123, 203
Fermi-LAT Collaboration. 2013, ArXiv e-prints:1303.2908
Fitzpatrick, G., Connaughton, V., McBreen, S., & Tierney, D. 2011
Geant4 Collaboration, Agostinelli, S., Allison, J., et al. 2003, Nuclear Instruments and Methods in Physics Research A, 506, 250
Gehrels, N. 1986, ApJ, 303, 336
Gopalswamy, N., Yashiro, S., Michalek, G., et al. 2009, Earth Moon and Planets, 104, 295
Hughes, E. B., Hofstadter, R., Rolfe, J., et al. 1980, IEEE Transactions on Nuclear Science, 27, 364
Kanbach, G., Bertsch, D. L., Fichtel, C. E., et al. 1988, Space Sci. Rev., 49, 69
—. 1993a, A&AS, 97, 349
—. 1993b, A&AS, 97, 349
Lin, R. P., Dennis, B. R., Hurford, G. J., et al. 2002, Sol. Phys., 210, 3
Meegan, C., Lichti, G., Bhat, P. N., et al. 2009, ApJ, 702, 791
Murphy, R. J., Dermer, C. D., & Ramaty, R. 1987, ApJS, 63, 721
Murphy, R. J., Share, G. H., Letaw, J. R., & Forrest, D. J. 1990, ApJ, 358, 298
Nakajima, H., Nishio, M., Enome, S., et al. 1995, Journal of Astrophysics and Astronomy Supplement, 16, 437
Neupert, W. M. 1968, ApJ, 153, L59
Ohno, M., Takahashi, H., Tanaka, Y. T., et al. 2011, The Astronomer's Telegram, 3635, 1
Omodei, N., Longo, F., Share, G., et al. 2012, in American Astronomical Society Meeting Abstracts, Vol. 220, American Astronomical Society Meeting Abstracts 220, 424.03
Omodei, N., Vianello, G., Pesce-Rollins, M., Allafort, A., & Gruber, D. 2011, The Astronomer's Telegram, 3552, 1
Pelassa, V., Preece, R., Piron, F., et al. 2010, ArXiv e-prints
Petrosian, V., Chen, Q., Giglietto, N., et al. 2012, in American Astronomical Society Meeting Abstracts, Vol. 220, American Astronomical Society Meeting Abstracts 220, 424.04
Petrosian, V., & Liu, S. 2004, ApJ, 610, 550
Ramaty, R., Murphy, R. J., & Miller, J. A. 1990, in American Institute of Physics Conference Series, Vol. 203, Particle Astrophysics - The NASA Cosmic Ray Program for the 1990s and Beyond, ed. W. V. Jones, F. J. Kerr, & J. F. Ormes, 143–154
Rank, G., Ryan, J., Debrunner, H., McConnell, M., & Schönfelder, V. 2001, A&A, 378, 1046
Reames, D. V. 1995, Advances in Space Research, 15, 41
Ryan, J. M. 1986, Sol. Phys., 105, 365
Tanaka, Y. T., Omodei, N., Giglietto, N., et al. 2012, The Astronomer's Telegram, 3886, 1
Thompson, D. J., Fichtel, C. E., Kniffen, D. A., & Ogelman, H. B. 1975, ApJ, 200, L79
Thompson, D. J., Bertsch, D. L., Fichtel, C. E., et al. 1993, ApJS, 86, 629
Trottet, G., & Vilmer, N. 1984, Advances in Space Research, 4, 153
Vestrand, W. T., Forrest, D. J., Chupp, E. L., Rieger, E., & Share, G. H. 1987, ApJ, 322, 1010
Vilmer, N. 1987, Sol. Phys., 111, 207